



# On the subsonic near-wake of a space launcher configuration without jet

Experimental investigation by means of particle image velocimetry (PIV) on the subsonic (Mach 0.5 to 0.9) near-wake flow of a space launcher configuration

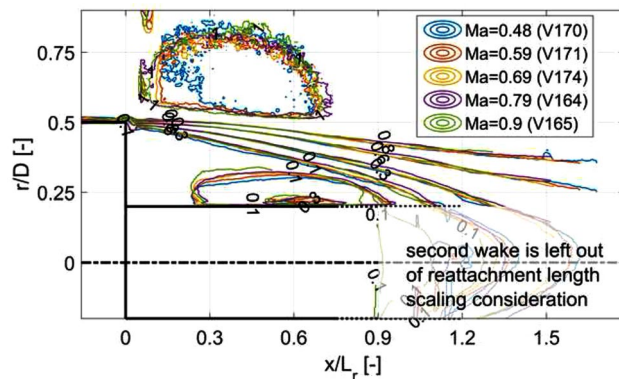
Dominik Saile<sup>1</sup> · Viktor Kühl<sup>1</sup> · Ali Gültan<sup>1</sup>

Received: 28 November 2017 / Revised: 13 November 2018 / Accepted: 09 January 2019  
© The Author(s) 2019

## Abstract

Wake flows have been extensively investigated in the past mainly with the objective to reduce drag. The failure of Ariane 5 Flight 157 though revealed that the understanding has not been sufficient, which triggered a new series of base-flow investigations. Most of them scrutinized the dynamics of the flow at one specific point along the flight path either in the subsonic, transonic, or supersonic range. However, no coherent image of the flow topology development in terms of a parametric study is available so far. The current work addresses the question of a near-wake scaling of a generic space launcher configuration. This question is tackled experimentally by means of particle image velocimetry measurements in the vertical test section Cologne in the range of Mach 0.5, 0.6, 0.7, 0.8, and 0.9 for Reynolds numbers between  $Re_D = 0.8 \times 10^6$  and  $1.7 \times 10^6$ . Results show the mean, the turbulence intensity, and the Reynolds shear stress distribution in the wake in comparison with the literature. In addition, data to the incoming boundary layer are provided and to the evolving shear layer. In that regime, the results indicate that the velocity and Reynolds stresses might be independent from the Mach and Reynolds number if scaled with the reattachment length. If this hypothesis holds true, it might be useful for the validation of numerical codes and for the initial determination of the flow field of space launchers in the design phase.

## Graphical abstract



## 1 Introduction

**Electronic supplementary material** The online version of this article (<https://doi.org/10.1007/s00348-019-2690-9>) contains supplementary material, which is available to authorized users.

Extended author information available on the last page of the article

Wake flows have been extensively investigated in the past mainly with the objective to reduce drag for which a large number of works are reviewed and gathered in Murthy and

Osborn (1976). The failure of Ariane 5 Flight 157 in 2002 though revealed that the understanding has not been sufficient, which triggered a new series of base-flow investigations. The flow regime of interest is transonic, since this is where the launcher is exposed to strong unsteady loads. Schwane (2015) reports pressure fluctuations with increasing amplitude for the first 37 s of the Ariane 5 Flight A501. David and Radulovic (2005) present pressure measurements taken during flight, which show that the strongest and most distinct frequency of Ariane 5 loads on the main engine occur for Mach 0.8. Measured loads on the actuator and accelerometers placed on the nozzle support the finding that the transonic flow regime is challenging with respect to the dynamics of the wake. Lately, a lot of attention has been put on revealing the governing instability mechanisms and the modes of the excitations (e.g., Weiss et al. 2009; Meliga et al. 2010; Schrijer et al. 2014; Statnikov et al. 2016; Statnikov 2016).

Most investigations focus on that critical, but narrow Mach number range along the trajectory at about 0.7–0.8. A broader view in terms of flow regime has been provided by Scharnowski et al. (2016) and Nadge and Govardhan (2014) who both conducted PIV measurements in the subsonic range for a two-dimensional backward-facing configuration. Scharnowski et al. (2016) extended the investigated range to the supersonic flow regime and combined the backward-facing step with a planar jet as representation of the exhaust jet of a launch system. The current study presents the PIV results of the flow field around a generic two-stage axisymmetric backward-facing step configuration, or, in other words, a space launcher configuration without a jet, exposed to an ambient flow ranging from Mach 0.5 to 0.9. The results are analyzed with respect to the mean-flow quantities and the Reynolds shear stresses. Furthermore, since the nature, scale, and intensity of the turbulence structure in the shear layer, after separation, is dependent upon the shear-layer initial conditions (Adams and Johnston 1988), and since the global dynamics (Deck and Thorigny 2007) of the recirculation region is influenced by this subsequent evolving shear layer, data are given for both and compared to results in the literature. Comparisons to literature are also drawn for the features of the recirculation region. The comparisons for the latter are mainly based on the study by Weiss et al. (2009), the configuration of which is very much comparable to the current one.

The following aspects are addressed in this study and can be declared as objectives: First, the applicability of the vertical test section Cologne (VMK) for base-flow experiments is targeted by verifying the results with literature. This is of importance, since it provides a foundation for the future base-flow experiments with hydrogen/oxygen combustion while taking advantage of the newly built hot plume testing facility of VMK (Saile et al. 2015). The second goal is to

capture and analyze data concerning the flow topology and the Reynolds stresses in the subsonic flow regime for numerical validation. The results also serve as background for the interpretation of the base pressure measurements, which have been captured during this measurement campaign, but are not presented in the frame here. Questions like what is the influence of an open or closed recirculation region on the pressure spectrum can then be discussed. Finally, differences to the other base-flow studies are targeted.

One of the open questions is the dependence on the Reynolds and Mach number of the velocity and Reynolds stress field in the near wake of the axisymmetric generic launcher (with no jet). Regarding similarity and scaling laws of axisymmetric wake flows, Uberoi and Freymuth (1970) stated that, in the near wake, the nature of turbulence depends on the shape of the corresponding body. Uberoi and Freymuth (1970) further elaborates that, farther downstream, the wake becomes dynamically self-similar. For the near-wake flow, Roshko and Lau (1965) investigated the reattachment process of backward-facing steps by means of pressure measurements. They introduced a scaling based on the reattachment length and the normalized pressure, which resulted in a collapse of the reattachment pressure-rise curve independently of the state of the boundary layer, meaning that it is valid for incoming laminar, transitional, and turbulent boundary layers. Westphal et al. (1984) confirmed this observation with the restriction to 'thin' boundary layers, which Adams and Johnston (1988) refined further pointing out that the reattachment point is independent of the ratio of boundary layer thickness  $\delta_{99}$  if the ratio to the step height  $h$  is smaller than 0.4. Besides for the spatial scaling, the reattachment length is also being used in the literature in a temporal sense for the non-dimensionalization of occurring frequencies. It was suggested by Mabey (1972) as scaling length for pressure fluctuations in separated flows. Merz et al. (1978) discovered that the centerline velocity distribution of a blunt body's axisymmetric near-wake exhibits a similar form throughout the subsonic range ( $0.11 < Ma < 0.94$ ). More recently, Nadge and Govardhan (2014) showed, for the flow over a backward-facing step and large Reynolds numbers ( $Re_h > 36,000$ ), that the separation region is nearly independent of Reynolds number. By means of PIV measurements, similarity was found with respect to normalized mean velocity field and the normalized turbulent stresses. Note that no clear division was made in the literature research above between axisymmetric and planar backward-facing step configuration, which is justified due to comparable effects and similarities. The similarity between the two with respect to some flow properties has been addressed or used for comparisons before, for instance, by Deck and Thorigny (2007) and Statnikov et al. (2017).

The following section (Sect. 2) describes the methods, meaning the measurement environment including the wind

tunnel, the model, the measurement techniques, and the evaluation methods. The results and discussion Sect. 3 addresses the boundary layer flow (Sect. 3.1), the wake flow (Sect. 3.2), and the evolution of the shear layer (Sect. 3.3). Comparisons to the literature data are presented in each section at the end. Finally, the study summarizes the conclusions and provides an outlook in Sect. 4.

## 2 Methods

The experiments are executed in the vertical test section Cologne (VMK). As shown in Fig. 1, VMK is a blow-down type wind tunnel featuring a vertical free test section for tests in the subsonic to supersonic range starting from Mach 0.5 up to 3.2. The current experiments were conducted with a subsonic 340 mm nozzle.

The wind tunnel model integrated in the subsonic wind tunnel nozzle is shown as a sketch in Fig. 2. The main components of this configuration are two co-axially aligned cylinders on top of each other. The first has a diameter of  $D = 66.7$  mm and the second  $d = 26.8$  mm. The smaller cylinder features a length of  $L = 80$  mm. This cylinder is actually a conical nozzle, which was closed with a plug at position ‘c’ for the study at hand. The geometry mimics the main generic components of the Ariane 5 base with respect to its scaling ( $d/D \sim 0.4$ ,  $L/D \sim 1.2$ ). Furthermore, the base plate is 10.4 mm downstream from the wind tunnel nozzle exit.

Upstream of the wind-tunnel nozzle exit, the wind-tunnel nozzle (1) is equipped with support arms (2) and (3), which have two tasks: First, they keep the wind-tunnel model in

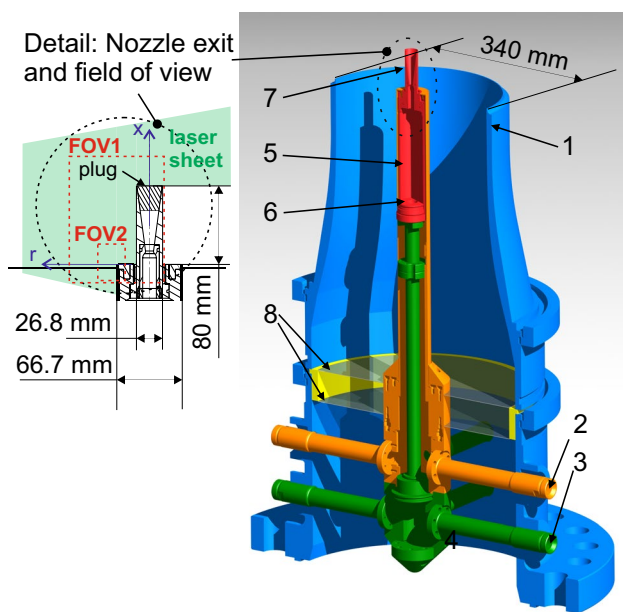


**Fig. 2** Sketch of the wind-tunnel model with the wind-tunnel nozzle (blue), cold jet supply system (green), and the chamber (red). The location in the frame of the facility is given in Fig. 1. The graph further contains the field of views, which are used for the base and boundary-layer flow investigations. They are denoted as FOV1 and FOV2, respectively

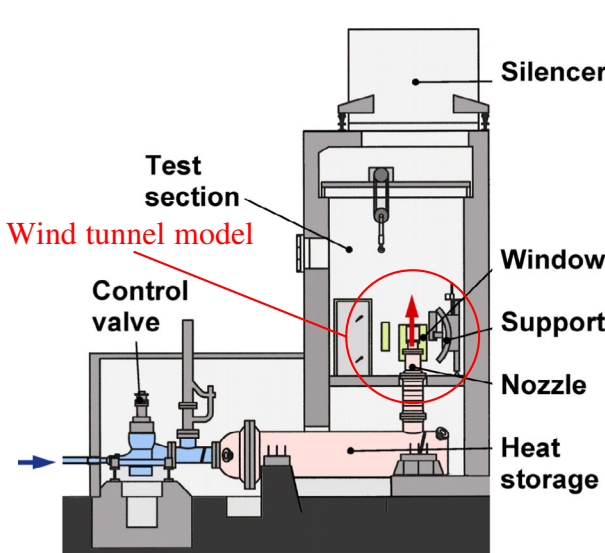


**Fig. 1** Schematic sketch of the VMK facility. The location of the wind tunnel model is encircled (in red) and the details of which are given in Fig. 2

place, and second, one or several supports can be used as access point for the harnessing of the sensors. The support arms converge in a central mounting (4) on top of which is the combustion or reservoir chamber (5). The injector (6) and the nozzle (7) are exchangeable to realize various injection conditions and nozzle exit conditions, respectively. The wind-tunnel nozzle is equipped with two levels of straighteners (8) downstream of the support arms to minimize perturbations.

The inflow conditions are listed in Tables 1 and 2. In detail, Table 1 contains the exit Mach number  $Ma_C$ , exit velocity  $U_C$ , and exit Reynolds number  $Re_D$  based on the diameter of the main cylinder  $D$ . Table 2 provides further parameters to which are successively referred in the corresponding sections. The exit Mach number was calculated under the assumption of an isentropic expansion by means of the reservoir and ambient pressure; the velocity is directly

**Table 1** Free-stream conditions for the FOV1 evaluation

| Run ID | $Ma_C$ | $U_C$ (ms <sup>-1</sup> ) | $Re_D$            |
|--------|--------|---------------------------|-------------------|
| V170   | 0.48   | 158.4                     | $0.8 \times 10^6$ |
| V171   | 0.59   | 192.7                     | $1.0 \times 10^6$ |
| V174   | 0.69   | 225.2                     | $1.2 \times 10^6$ |
| V164   | 0.79   | 256.8                     | $1.4 \times 10^6$ |
| V165   | 0.90   | 285.8                     | $1.7 \times 10^6$ |

**Table 2** Free-stream conditions and parameters with respect to the inflow boundary layer at  $x/D = -0.15$  of the *FOV2* evaluation

| Run ID | $Ma_C$ | $U_C$ ( $\text{ms}^{-1}$ ) | $\frac{u_{\text{rms},C}}{U_C}$ | $Re_D$            | $\delta^*/h$ | $\theta/h$ | $H$  | $\delta_{99}/h$  | $u^*$ ( $\text{ms}^{-1}$ ) | $\Pi$ |
|--------|--------|----------------------------|--------------------------------|-------------------|--------------|------------|------|------------------|----------------------------|-------|
| V114   | 0.61   | 195.9                      | 3.5                            | $1.1 \times 10^6$ | 0.027        | 0.021      | 1.31 | $0.32 \pm 0.014$ | 8.0                        | -0.12 |
| V116   | 0.71   | 227.0                      | 3.0                            | $1.3 \times 10^6$ | 0.030        | 0.020      | 1.54 | $0.29 \pm 0.011$ | 9.1                        | -0.03 |
| V117   | 0.81   | 253.8                      | 2.8                            | $1.5 \times 10^6$ | 0.025        | 0.016      | 1.59 | $0.23 \pm 0.012$ | 10.2                       | -0.02 |
| V119   | 0.91   | 287.6                      | 2.4                            | $1.7 \times 10^6$ | 0.027        | 0.016      | 1.67 | $0.25 \pm 0.012$ | 11.4                       | 0.01  |

The boundary-layer thickness is additionally provided with the bounds for the 95% confidence interval determined by means of a Monte Carlo simulation

taken from the PIV results. The boundary-layer velocity profile is extracted at a location directly downstream of the wind-tunnel nozzle exit ( $x/D = -0.15$ ), which is the location the least affected from upstream effects of the base-flow dynamics. Due to corrupt results just upstream of the base for the investigation of the wake flow, the ambient flow (Table 1) had to be determined farther downstream from the base. The ambient flow is averaged over an area between  $0.15 < x/D < 0.2$  and  $0.7 < r/D < 0.8$ .

For the PIV measurements, a classical 2D–2C setup was chosen. For the laser sheet generation, the laser system Ultra CFR Nd:YAG by Big Sky Laser, now Quantel Ltd., was used. Each laser pulse has an energy of 190 mJ at a wavelength of 532 nm. The sheet thickness was in the range of 0.5 mm. Perpendicular to the laser sheet, a PCO1600 camera system by PCO AG was set up at a distance of about 180–200 mm for the acquisition of the particle images. The LabSmith timing unit by LC880 controls the trigger pulses for both components with an accuracy of 100 ps. Dependent on the focus of the experiments, the camera was equipped with either of two different lenses by Carl Zeiss AG to resolve two different fields of views (FOV). The Distagon  $T^*2/35$  ZF was used for a global view of the wake featuring a FOV (labeled *FOV1*) of about  $134 \times 100 \text{ mm}^2$ . The aperture number was set to 16. The Makro-Planar 2/100 ZF was applied for boundary-layer measurements with an aperture number setting of 11. In hindsight, the aperture setting turned out to be too large. As a result of the large depth of field, the raw images for the *FOV1* setting captured the background of the nozzle, which obviously affected the correlation-based evaluation. Thus, the data of incoming flow region are erroneous for the *FOV1*. The corresponding range is exemplarily marked with excl. (for excluded) in Figs. 5, 10 and 13. The setting provided a FOV of  $30.9 \times 23 \text{ mm}^2$ , which is equivalent to an increase of the resolution by a factor of 4.3. The latter is labeled *FOV2*. Both FOVs are depicted in Fig. 2, which also show the coordinate system originating in the symmetry axis on the base. Titanium dioxide of the type K1002 from Kronos International, Inc. is used as seeding material.

The analysis of the dual-frame/single-exposure images was executed with PIVview V3.60 by PIVTEC GmbH. For the image sampling, various interrogation window sizes have

been tested in a sensitivity study. For both FOVs, the multi-grid interrogation method with grid refinement was applied, the Whittaker reconstruction (Raffel et al. 2013) was used for the sub-pixel peak fit, and on the final pass, a B-spline interpolation scheme of 3rd order was applied to cover the aspect of adaptive image deformation. The data were not interpolated.

For the wake-flow investigations (*FOV1*, Run ID: V170, V171, V174, V164, V165), 345 images were available per run. A sensitivity study led to an interrogation window size of  $32 \times 16 \text{ px}$  ( $2.68 \times 1.34 \text{ mm}^2$ ) with an overlap of  $4 \times 4 \text{ px}$ . Note that the free-stream particle displacement for the runs with *FOV1* was about 8 px.

For the boundary-layer flow (*FOV2*, Run ID: V114, V116, V117, V119), a total number of 694 images were captured per run. The interrogation window size was chosen by taking the signal-to-noise ratio into account, which led to  $32 \times 16 \text{ px}$  ( $0.62 \times 0.31 \text{ mm}^2$ ) with an overlap of  $4 \times 4 \text{ px}$ . The free-stream displacement for *FOV2* is about 8 px for run ID V114 and about 10 px for the rest. For this magnification, the movement between the camera and the wind-tunnel model was actually notable and has been corrected. If it is assumed that the camera is standing still, it can be interpreted as a measure for the wind-tunnel model oscillation. The results show that the oscillations are small, meaning that the standard deviation of the lateral motion is in the range between 70 and 110  $\mu\text{m}$ .

One objective of the close-up (*FOV2*) data is the analysis of the incoming boundary-layer properties. For that reason, the profile up to 98% of the edge velocity  $u_e$  is used for a fitting (Berg 1977) to the law of the wake (e.g., White 1991; Schetz and Bowersox 2011). The law of the wall including the wake (law of the wake) for incompressible turbulent boundary-layer flows is given in Eq. 1. Clauser's values (Clauser 1956) are used for  $\kappa$  and  $B$ , which are, in this case, equal to 0.41 and 4.9, respectively. The velocity  $u$  and the distance to the wall  $\Delta r$  are normalized to the dimensionless distance to the wall  $r^+$  and the dimensionless velocity  $u^+$  by means of the shear stress velocity  $u^*$  and the kinematic viscosity  $\nu$ , as shown in Eq. 2. The boundary-layer thickness is given by  $\delta_{99}$ , and for the description of the wake, a sine square ansatz with Coles' wake parameter  $\Pi$  is used (see, e.g., Schetz and Bowersox 2011). Furthermore, boundary

layer characterizing parameters are provided for comparison: Eqs. 3 and 4 describe the displacement thickness  $\delta^*$  and the momentum thickness  $\theta$ . The shape factor  $H$  is defined as the ratio between the two, and thus, it is  $H = \delta^*/\theta$ .

$$u^+ \approx \frac{1}{\kappa} \ln(r^+) + B + \frac{2\pi}{\kappa} \sin^2 \left( \frac{\pi}{2} \frac{\Delta r}{\delta_{99}} \right), \quad (1)$$

$$u^+ = \frac{u}{u^*}; \quad r^+ = \frac{\Delta r u^*}{v}, \quad (2)$$

$$\delta^* = \int_0^{\delta_{99}} \left( 1 - \frac{u}{U_C} \right) d\Delta r, \quad (3)$$

$$\theta = \int_0^{\delta_{99}} \left( 1 - \frac{u}{U_C} \right) \frac{u}{U_C} d\Delta r. \quad (4)$$

The in-succession evolving shear layer is characterized by the vorticity thickness. The vorticity thickness  $\delta_\omega$  is defined in Eq. 5 (Brown and Roshko 1974). For *FOV2*, the minimum velocity  $u_{\min}$  cannot be determined because it is not in the field of view. Then, it is assumed that  $u_{\min}$  is 34% of the maximum velocity  $u_{\max}$ , which is the average percentage of the minimum velocity derived from the *FOV1* experiments.

$$\delta_\omega = \frac{u_{\max} - u_{\min}}{\max(du/dr)}. \quad (5)$$

An uncertainty analysis has been conducted which is based on an approach suggested by Lazar et al. (2010). The analysis takes into account the equipment-related uncertainty, the uncertainty due to the particle lag, and the sampling uncertainty. The equipment-related uncertainty includes calibration and timing error. The approach for the calculation of the sampling uncertainty is extracted from Benedict and Gould (1996). The total uncertainty for *FOV1* is largest for the Mach 0.9-case and amounts to  $\pm 3.4$  with respect to the incoming flow velocity  $U_C$ . For *FOV2*, the uncertainty is in the range of  $\leq \pm 3.3\%$ . For the turbulent quantities, only the 95% confidence interval of the sampling uncertainty according to Benedict and Gould (1996) is provided as shading in the corresponding graphs. The confidence interval for boundary-layer thickness in Table 2 has been determined by means of a Monte Carlo simulation imposing the previously determined velocity uncertainty levels. The velocity uncertainty levels are equally used for the determination of the vorticity-thickness uncertainty in Sect. 3.3, which also incorporates an extrapolation of the higher resolved velocity gradient results from field of view *FOV2* to the results of *FOV1*. Furthermore, the results have been checked for peak-locking, which, in consequence, was ruled out, and with respect to the signal-to-noise ratio.

The latter has been assessed for the cross correlation of the interrogation windows and for two-point correlations of the velocity field in the region where turbulence is homogeneous, meaning in the streamwise direction of the boundary layer.

### 3 Results and discussion

#### 3.1 Inflow conditions and upstream boundary layer

The upstream boundary layer plays a key role in the development of the subsequent wake flow and is, consequently, described in the following. Figure 3 shows the mean-flow results in inner scaling as least-square fit to the law of the wake (Eq. 1) for Mach  $\sim 0.6$  to  $\sim 0.9$ . For comparison, the law of the wall and the law of the wake for a two-dimensional flat plate without pressure gradient are additionally plotted. The graph points at two outcomes: first, the fit to the logarithmic part of the law of the wall appears to be sound indicating that the boundary layer is presumably turbulent. Second, the boundary-layer profile does not exhibit the typical wake above the log layer. This can usually be found in environments with a favorable pressure gradient. Such a favorable pressure gradient environment is present upstream and downstream from the base region: Upstream due to the conditions imposed by the wind tunnel nozzle and downstream due to the low-pressure environment after the flow separation from the base (Deprés et al. 2004).

Figure 4 shows the radial profiles of the streamwise turbulence intensity for the different Mach numbers along with the findings by Klebanoff (1955). Outside of the boundary layer ( $\Delta r/\delta_{99} > 0.5$ ), the turbulence is

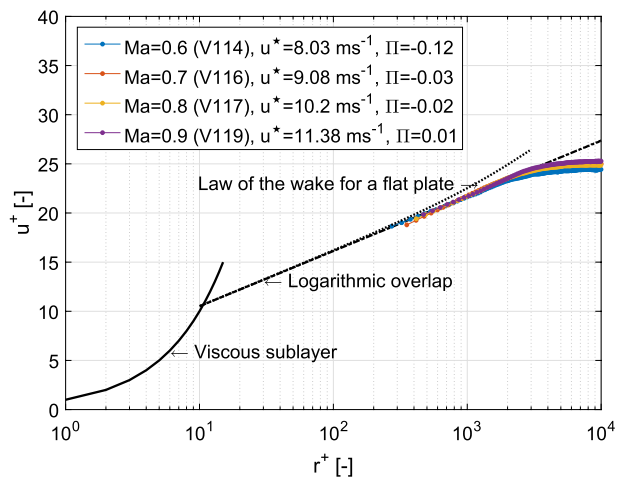


**Fig. 3** Boundary-layer profiles of the investigated inflow Mach numbers fitted to the law of the wall with wake. The law of the wake for the flat plate is based on  $\Pi = 0.51$ ,  $u^* = 11.38 \text{ ms}^{-1}$ , and  $\delta_{99} = 4.9 \text{ mm}$

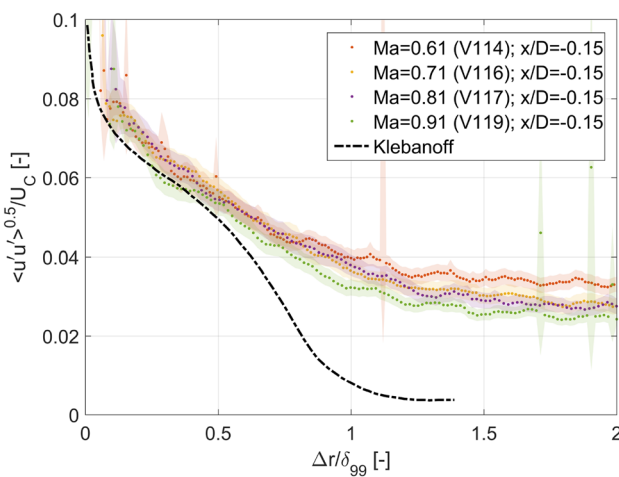


**Fig. 4** Turbulence intensity profiles of the boundary layer

dominated by the inflow conditions imposed by the test environment. When approaching the wall ( $\Delta r / \delta_{99} < 0.5$ ), one can discover a transition close to the trend of Klebanoff (1955). Between  $0.1 < \Delta r / \delta_{99} < 0.5$ , the largest mean deviation is found for the Mach 0.8-case, which amounts to  $\Delta \langle u'u' \rangle^{0.5} / U_C = 0.0061$ . Very close to the wall at about  $\Delta r / \delta_{99} < 0.1$ , the velocity fluctuations increase due to random noise.

These findings are quantified in Table 2. It lists Coles wake parameter  $\Pi$  for the corresponding test runs at  $x/D = -0.15$ . The least-square fitting procedure finds values close to zero, which most likely reflects the strong negative (favorable) pressure gradient. Furthermore, the table contains the second fitting parameter, namely the shear stress velocity  $u^*$ .

Obviously, the fitting required a preceding determination of the mean velocity profile. Inherent data like the edge velocity  $U_e$ , which is equivalent to the free-stream velocity  $U_C$ , the boundary-layer thickness  $\delta$ , the displacement thickness  $\delta^*$ , and the momentum loss thickness  $\theta$ , have been extracted, and are presented in the same table as ratio to the height  $h$ . The last parameter in the table reflects the incoming axial turbulence intensity  $\langle u'u' \rangle^{0.5} / U_C$  from the VMK test environment in the streamwise direction as it can also be extracted from Fig. 4 outside of the boundary layer.

The high level of incoming velocity fluctuations rises the question of its impact on the base flow. This will be addressed in Sect. 3.2.4 where a comparison to the literature is given. First, though, the study focuses on the base flow as evolving in the current environment.

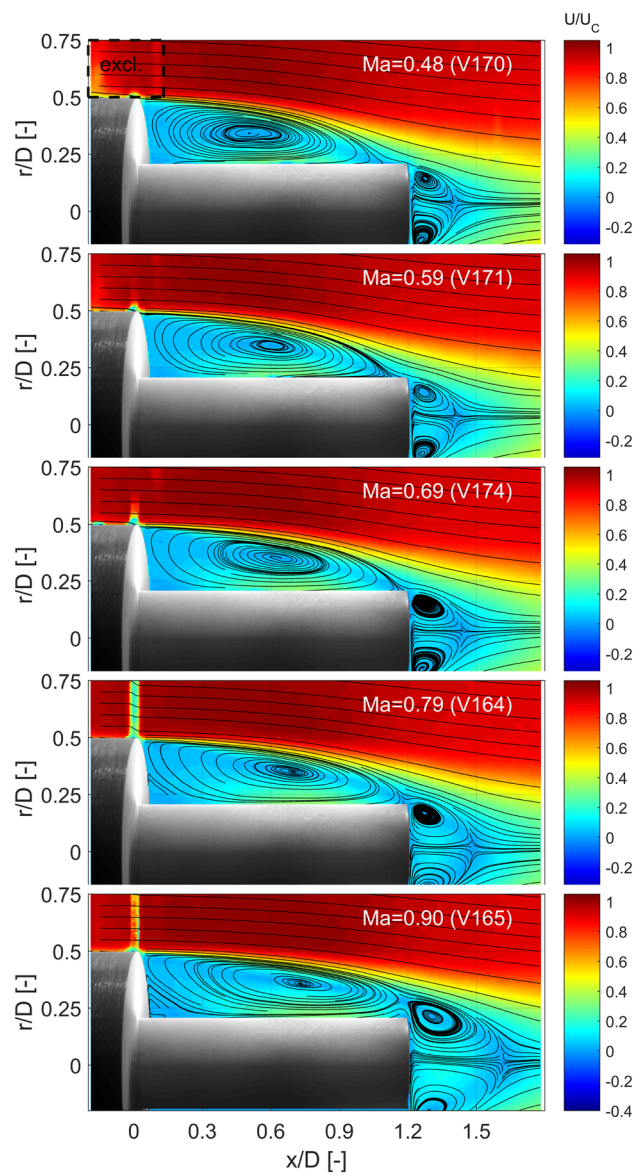


**Fig. 5** Contour plots with streamlines of the mean-flow field for  $Ma = 0.48, 0.59, 0.69, 0.79, 0.9$

### 3.2 Wake-flow and Mach number dependence

The wake flow and its dependence to the Mach number is assessed in the following. In the frame of that, the flow field is scaled by means of the reattachment length as first suggested by Roshko and Lau (1965) with the objective to scrutinize the current configuration for flow similarity.

#### 3.2.1 Mean velocity distribution

A contour plot of the dimensionless mean flow with the corresponding streamlines is shown for all the investigated Mach numbers in Fig. 5. The characteristic flow features of

an axisymmetric backward-facing step flow like flow separation from the shoulder, reattachment on the dummy nozzle, and the enclosed recirculation vortex between the base and the dummy nozzle are clearly visible. Up to Mach 0.7, the streamlines indicate that the flow reattaches on average on the nozzle dummy. For Mach 0.8, the reattachment appears ambiguous. It seems like the recirculation region in the base of the main body and farther downstream in the wake of the dummy nozzle are connected. The merging of the two wake regions becomes more obvious for Mach 0.9. Along with the reattachment location, the location of the vortex center moves equally farther downstream for higher Mach numbers.

Furthermore, the wake-flow downstream of the dummy nozzle is asymmetric possibly indicating a slight misalignment or angle of attack of the wind tunnel model with respect to the ambient flow. Efforts with respect to its adjustment were undertaken, but this degree misalignment was finally accepted due to the strong sensitivity. The asymmetry is more pronounced for the lower Mach number range and straightens out for the larger Mach number. A strong sensitivity to an angle of attack has been noticed in the past in the low subsonic regime in the investigation by Wolf (2013). There, it was shown that a misalignment with an angle of attack as small as  $0.35^\circ$  leaves a notable impact on the flow field symmetry.

Characteristic elements of the wake flow, specifically the location of reattachment and center of the main vortex, are listed in Table 3. These results agree well the findings by Lê (2005). For an upstream supported model with the same geometrical proportions, Lê (2005) found the following reattachment lengths:  $L_r/D = 1.07, 1.09, 1.126$ , and  $1.143$  at Mach 0.5, 0.6, 0.7, and 0.77, respectively. For a very long cylindrical rear body and an ambient flow at Mach 0.8, Deprés et al. (2004) report a relative reattachment length of 1.3. Reattachment lengths of further axisymmetric backward-facing step configurations are given in Table 4. A good

agreement is also found for the unperturbed case of Weiss and Deck (2013) where a value of 1.14 is given for Mach 0.7. In general, the current reattachment lengths are well in the range of the data presented in Table 4.

Furthermore, over the course of the paper at hand, an attempt is made to scale the near-wake flow with the reattachment length. Obviously, this is only feasible if the mean reattachment location can actually be found on the solid wall of the nozzle dummy. This is not the case for the Mach 0.9-case. For this case, a fictive reattachment length is approximated based on the ratio between the axial position of the vortex center and the reattachment length found for the previous cases. As baseline, the ratio of the Mach 0.6- and 0.7-case is used, which appears to unambiguously reattach on the solid dummy nozzle.

Now, the contour plot can be scaled with respect to the reattachment length. Figure 6 shows normalized iso-contour lines of the velocity scaled with the base diameter. This graph depicts again the observation from above: The larger the Mach number, the more elongated is the recirculation bubble and the farther downstream are the center of the bubble and the reattachment location. If the velocity field is now scaled in the streamwise direction with the reattachment length as given in Table 3, the iso-contour velocity lines nearly coincide (Fig. 7). It appears like the current near-wake flow exhibits self-similar characteristics in the range above the solid nozzle wall ( $r/D \geq 0.2$ ) for a reattachment length-based scaling.

A discrepancy can be noted in the wake of the dummy nozzle for which the current scaling approach does not apply. This presumably poses a 'new' situation with a blunt axisymmetric body. For blunt axisymmetric bodies, Merz et al. (1978) found similarity with respect to the centerline velocity distributions for subsonic Mach numbers. However, the second wake is out of the scope of the current work and not pursued further here.

The hypothesis regarding the scaling with the reattachment length is further scrutinized by comparing the streamwise and counter-streamwise velocity profiles at one position inside the recirculation bubble (Fig. 8) and one position downstream from the reattachment (Fig. 9). Another objective of the profiles is to provide quantitative data for comparisons.

It shows that the profiles of the various Mach number concur with moderate deviations. For instance, if the Mach 0.8-case is taken as reference, one finds the largest difference to one of the other profiles for the Mach 0.9-case for both locations. On average, it amounts to  $|\Delta u|/U_C \leq 0.024$  and to  $|\Delta v|/U_C \leq 0.01$  between  $0.25 \leq r/D \leq 0.75$  for that case. Note that the lower radial distance of about  $r/D = 0.25$  was chosen to accommodate for the differences due to the reattachment process (solid/fluidic). Moreover, it appears that the 'fictive' reattachment scaling as done for the overshooting Mach 0.9-case

**Table 3** Location of vortex center, reattachment, and the ratio between both

| Run ID | Mach number ( $Ma_C$ ) | Recirc. region center ( $x_{vc}/D, r_{vc}/D$ ) | Reattach. length ( $L_r/D$ ) | Ratio ( $x_{vc}/L_r$ ) |
|--------|------------------------|--|------------------------------|------------------------|
| V170   | 0.48                   | [0.51, 0.35]                                   | 1.06                         | 0.48                   |
| V171   | 0.59                   | [0.61, 0.35]                                   | 1.11                         | 0.545                  |
| V174   | 0.69                   | [0.64, 0.35]                                   | 1.17                         | 0.55                   |
| V164   | 0.79                   | [0.70, 0.35]                                   | 1.18                         | 0.596                  |
| V165   | 0.90                   | [0.75, 0.36]                                   | 1.36*                        | 0.548                  |

The vortex center and fictive reattachment length is denoted by the subscript "vc" and the superscript "\*", respectively. The italic value for the  $x_{vc}/L_r$  denotes that it is built with the fictive reattachment length  $L_r/D = 1.36$

$L_r$  denotes the reattachment length and  $x_{vc}$  denotes the axial position of the vortex center

**Table 4** Overview to commonalities and differences of comparable studies

| Reference   | Scharnowski et al. (2015) | Scharnowski et al. (2015) | Schrirjer et al. (2014) | van Gent et al. (2017) | Weiss and Deck (2013) | Weiss and Deck (2013; P) | Weiss and Deck (2013; U)      | Curr. study 1 | Curr. study 2 |
|---|---------------------------|---------------------------|-------------------------|------------------------|-----------------------|--------------------------|-------------------------------|---------------|---------------|
| Mach number $Ma_C$  | 0.7                       | 0.7                       | 0.7                     | 0.76                   | 0.7                   | 0.7                      | 0.7                           | 0.7           | 0.8           |
| Reynolds number $Re_D \times 10^{-6}$                           | 1.0                       | 1.0                       | 1.3                     | 1.5                    | 1.2                   | 1.2                      | 1.2                           | 1.4           | 1.7           |
| Method approach   | Exp./PIV                  | CFD/LES                   | Exp./PIV                | Exp./PIV               | Exp./LDV              | CFD/ZDES                 | CFD/ZDES                      | Exp./PIV      | Exp./PIV      |
| Environment   | Closed TS                 | Free-stream               | Closed TS               | Closed TS              | Open TS               | Open TS                  | Free-stream                   | Open TS       | Open TS       |
| Forebody  | Yes                       | Yes                       | Yes                     | Yes                    | No                    | No                       | No                            | No            | No            |
| Base geom.  |                           |                           |                         |                        |                       |                          |                               |               |               |
| L/D   | $\infty$                  | $\infty$                  | 2.54                    | 2.54                   | 1.2                   | 1.2                      | 1.2                           | 1.2           | 1.2           |
| d/D   | 0.4                       | 0.4                       | 0.33                    | 0.33                   | 0.4                   | 0.4                      | 0.4                           | 0.4           | 0.4           |
| Nozzle simulation   | Sting                     | Sting                     | DN                      | DN                     | DN                    | DN                       | DN                            | DN            | DN            |
| Support method  | Sting + strut             | None                      | Strut                   | Strut                  | Upstr.                | Upstr.                   | Upstr.                        | Upstr.        | Upstr.        |
| Inflow turbulence   |                           |                           |                         |                        |                       |                          |                               |               |               |
| $\frac{\langle u' u' \rangle^{0.5}}{U_c}$                       | n.a.                      | est. low                  | n.a.                    | est. low               | < 0.03                | ~ 0                      | $\lesssim 0.015$ at r/<br>D=1 | 0.030         | 0.028         |
| State of BL   | Turb.                     | Turb.                     | Trip./turb.             | Trip./turb.            | Est. turb.            | Turb.                    | Turb.                         | Turb.         | Turb.         |
| BL thick.   |                           |                           |                         |                        |                       |                          |                               |               |               |
| $\delta_{99}/D$   | 0.120                     | 0.100                     | 0.042                   | 0.06                   | n.a.                  | n.a.                     | n.a.                          | 0.086         | 0.067         |
| Ratio BL to step height   |                           |                           |                         |                        |                       |                          |                               |               |               |
| $\delta_{99}/h$   | 0.39                      | 0.33                      | 0.13                    | 0.18                   | n.a.                  | n.a.                     | n.a.                          | 0.29          | 0.23          |
| Wake param.   |                           |                           |                         |                        |                       |                          |                               |               |               |
| $\Pi$   | Est. ~ 0.51               | Est. ~ 0.51               | Est. ~ 0.51             | Est. ~ 0.51            | Est. ~ 0              | Est. ~ 0                 | Est. ~ 0.51                   | Fit: ~ 0      | Fit: ~ 0      |
| Reattach. length  |                           |                           |                         |                        |                       |                          |                               |               |               |
| $L_r/D$   | 1.06                      | 1.30                      | 1.0                     | 1.1                    | n.a.                  | 1.0                      | $\sim$ Pos. 9                 | 1.14          | 1.17          |
| Max. turb int.  |                           |                           |                         |                        |                       |                          |                               |               |               |
| $\left( \frac{\langle u' u' \rangle^{0.5}}{U_c} \right)_{\max}$ | n.a.                      | n.a.                      | > 0.22<br>< 0.24        | > 0.23<br>< 0.24       | 0.23                  | 0.21                     | 0.17                          | 0.18          | 0.19          |
| Max. Rey. shear stress  |                           |                           |                         |                        |                       |                          |                               |               |               |
| $-\left( \frac{\langle u' v' \rangle}{U_c^2} \right)_{\max}$    | $\gg 0.03$                | $> 0.03$                  | $\geq 0.026$            | n.a.                   | 0.024                 | 0.021                    | 0.014                         | 0.014         | 0.015         |

TS test section; BL boundary layer; n.a. not applicable or not available; est. estimated based on interpretation or educated guess; fit fitted to law of the wake; upstr. upstream; DN dummy nozzle; (U/P) un-/perturbed

is appropriate. In summary, there seem to be evidences for the argument of a reattachment length-scaled, mean self-similar base-flow topology. The question now is if the same observations can be made for the fluctuations.

### 3.2.2 Velocity fluctuation distribution

**Axial turbulence intensity** An overview to the fluctuation distribution is given first before addressing the presumable the reattachment length scaling of the flow field. The normalized turbulence intensity in the streamwise direction is given as contour plots in Fig. 10 for the investigated Mach

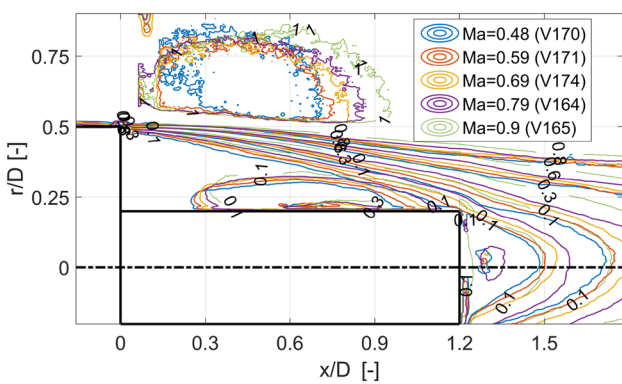


**Fig. 6** Iso-contour lines of the normalized mean velocity field scaled with the base diameter  $D$

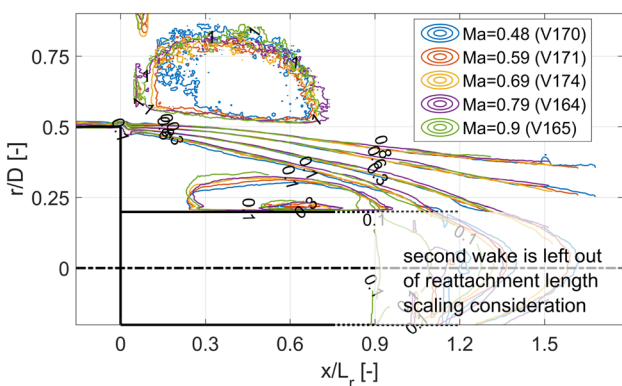


**Fig. 7** Iso-contour lines of the normalized mean velocity field scaled with the reattachment length  $L_r$

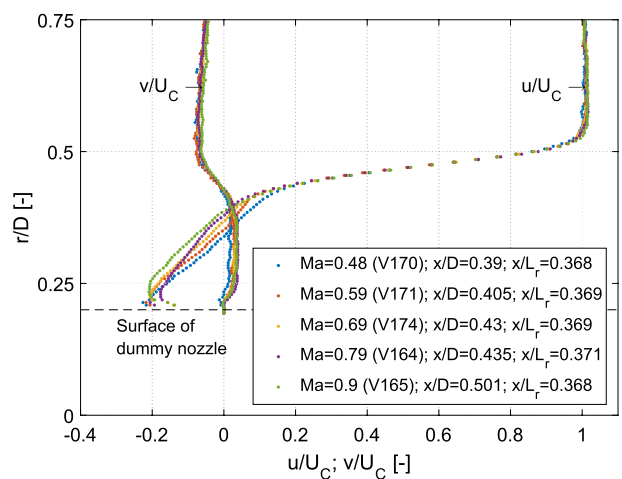


**Fig. 8** Normalized mean velocity profiles in the streamwise and radial direction for the location  $x/L_r = 0.37$

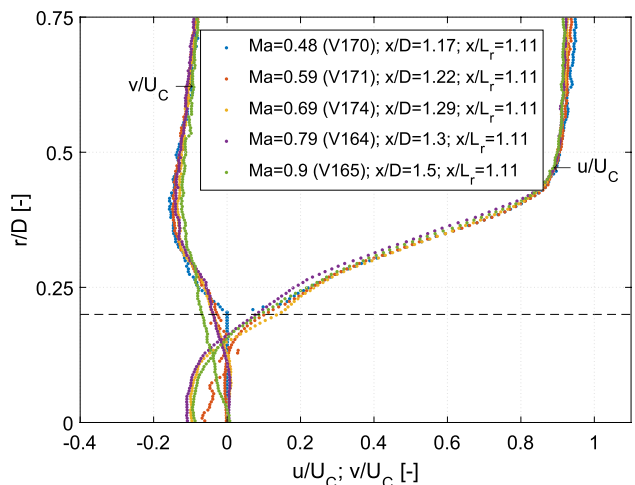


**Fig. 9** Normalized mean velocity profiles in the streamwise and radial directions for the location  $x/L_r = 1.1$

numbers. Two distinct areas with increased normalized turbulence intensity can be observed, which merge farther downstream. The first finger-like patch can be found in the shear layer and the second extends upstream from the main vortex center in the recirculation bubble. The merging location downstream from the recirculation center is in the vicinity where the normalized turbulence intensity is maximal. Higher Mach numbers exhibit larger normalized turbulence intensity levels. For instance, the maximal magnitude increases from about 0.14 to about 0.18 from Mach 0.5 to 0.9, respectively. Furthermore, the radial extension of increased turbulence covers a larger range in the radial direction for the two larger Mach numbers 0.8 and 0.9.

In the study by Scharnowski (2013), the distribution is described as two plateaus with a distinct valley between shear layer and the primary recirculation region. By analyzing of 350,000 vortices, Scharnowski (2013) concluded that a decreased likelihood for the occurrence of vortices in between the two regions is responsible for this valley. In addition, the vortices were categorized by their swirl strength into weak and strong swirls, which led to the finding that clockwise rotating vortices with (relatively) weaker swirl strength cause the second finger/the excited area in the recirculation bubble.

Radial slices of the normalized turbulence intensity are shown in Figs. 11 and 12 again to scrutinize the reattachment length-scaling concept and to provide data for comparison. Inside the recirculation bubble ( $x/L_r = 0.37$ ), this concept appears to apply: the turbulence intensity profiles inside the recirculation region ( $r/D < 0.5$ ) are similar within the sampling uncertainty for all Mach number.

This only partially holds true for the location downstream from the reattachment location. While the results still appear to be comparable between Mach 0.5 and 0.6, a deviation

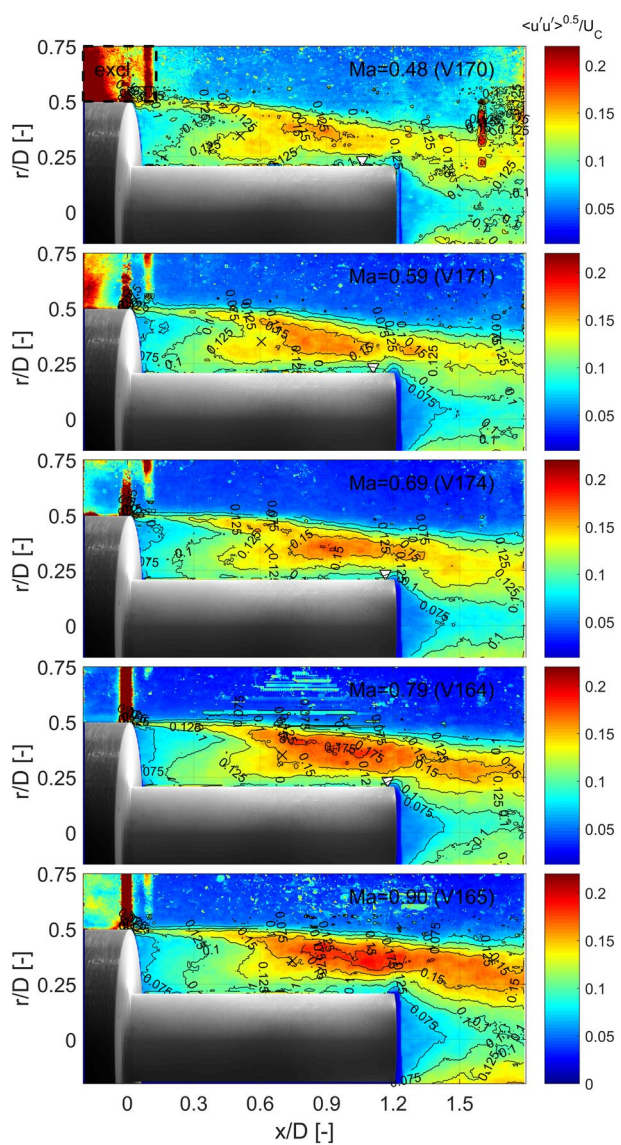


**Fig. 10** Contour plots of the normalized turbulence intensity field for  $Ma = 0.48, 0.59, 0.69, 0.79$ , and  $0.9$ . The center of the main vortex and the reattachment location are plotted as cross  $\times$  and as triangle  $\nabla$ , respectively

from that trend seems to become notable starting from Mach 0.7, which seems to be manifested further for and above Mach 0.8. This appears to correlate with the observation for reattachment process of the shear layer (see Fig. 5): Below Mach 0.6, the shear layer very likely impinges exclusively or predominantly on the solid nozzle wall. A hybrid state is evidenced for Mach 0.7 and 0.8 where the shear layer impinges intermittently on the solid nozzle wall and on the flow farther downstream. Remember that, for both of these Mach numbers, the mean reattachment location is found to be close to the edge (Table 3). Finally, for Mach 0.9, the shear layer appears to overshoot the dummy nozzle and a mutual interaction between the separated shear layers can

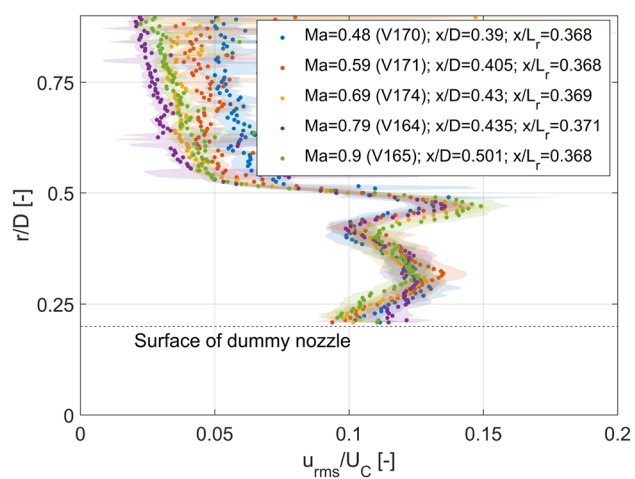


**Fig. 11** Normalized turbulence intensity profiles for the location  $x/L_r = 0.37$

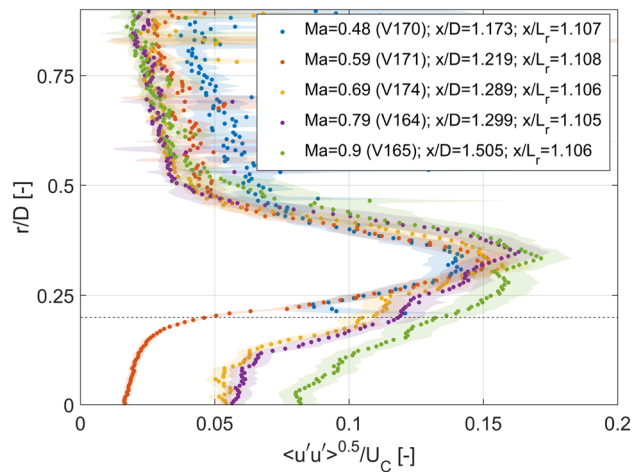


**Fig. 12** Normalized turbulence intensity profiles for the location  $x/L_r = 1.1$

take place, which is usually classified as fluidic reattachment (Deprés et al. 2004). These differences regarding the shear layer reattachment process might explain for deviating profiles farther downstream.

**Reynolds shear stress** The normalized Reynolds shear stress distribution is captured in Fig. 13. It resembles strongly the previously described turbulence intensity distribution with respect to regions of excitation. The finger-like patterns presumably describing the areas of increased turbulence are similarly found in the shear layer and inside the recirculation bubble, and again, the magnitude of the Reynolds shear stress increases with increasing Mach number. For Mach 0.5, the maximum is in the range of about 0.7% and increases to about 1.6% for Mach 0.9.

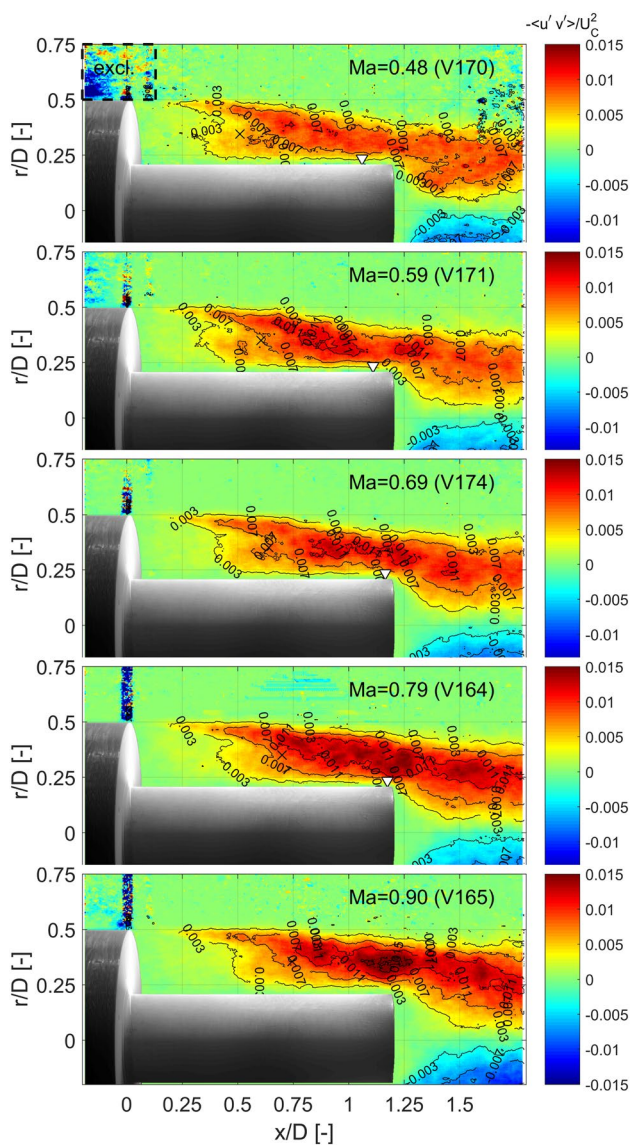


**Fig. 13** Contour plots of the normalized Reynolds shear stress field for  $Ma = 0.48, 0.59, 0.69, 0.79, 0.9$ . The center of the main vortex and the reattachment location are plotted as cross  $\times$  and as triangle  $\nabla$ , respectively

The distribution here indicates comparable self-similar traits as indicated by the turbulence intensity distribution. To provide a visual impression for that, an iso-contourline distribution is provided in the following as done for the mean velocity (see Fig. 7). For comparison, the distribution is given as base diameter and reattachment length-based scaling in Figs. 14 and 15, respectively. Due to higher level of noise, the results are more ambiguous in comparison to the mean-flow distribution. Nevertheless, the iso-lines reflecting the dynamics in the recirculation region seem to feature a comparable trend (see ellipse). In the second (nozzle dummy) wake though, at about  $x/L_r > 0.9$ , the iso-contour lines capture the dynamics of the second and independent wake.

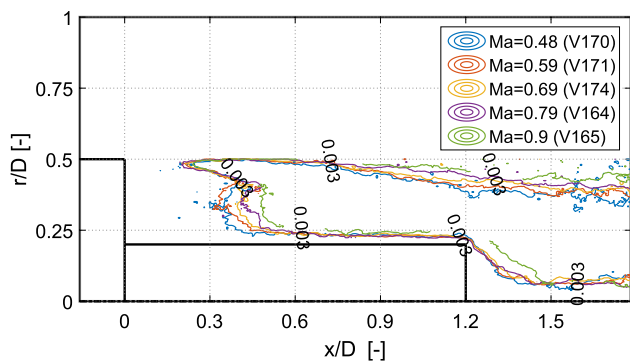


**Fig. 14** Iso-contour plot lines of the normalized Reynolds shear stress field scaled with the base diameter  $D$

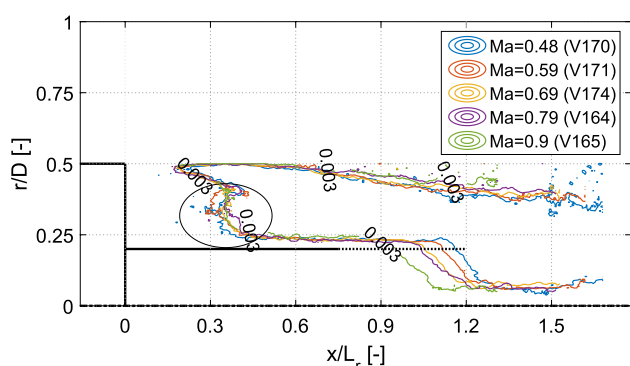


**Fig. 15** Iso-contour plot lines of the normalized Reynolds shear stress field scaled with the reattachment length  $L_r$

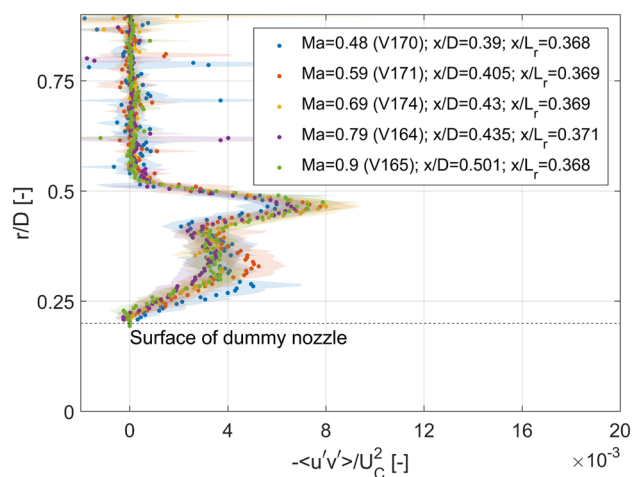


**Fig. 16** Normalized Reynolds shear stress profiles for the location  $x/L_r = 0.37$

Correspondingly, the shear stress profiles shown in Figs. 16 and 17 appear to exhibit the similar elements. Inside the recirculation bubble ( $x/L_r = 0.37$ ), the profiles indicate

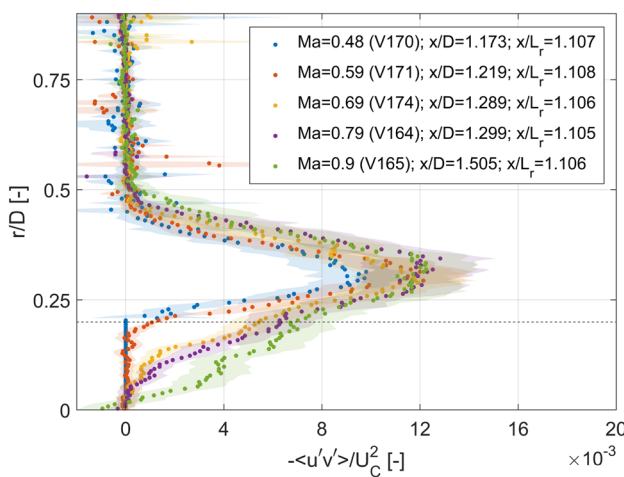


**Fig. 17** Normalized Reynolds shear stress profiles for the location  $x/L_r = 1.1$

self-similar traits. All Mach numbers exhibit a very comparable trend, e.g., with respect to the magnitude and location of the extrema. This characteristic appears to dissolve farther downstream. Above, it was suggested that this is due to the nature of shear-layer reattachment, meaning solid, hybrid, or fluidic.

### 3.2.3 Comment to reattachment length scaling

The question regarding similarity effects in the near-wake flow was elaborated in the introduction above. In short, similarity was found by the other researchers before for the near-wake flow in a wide-flow range if a scaling with the reattachment length (Roshko and Lau 1965; Mabey 1972) is applied. For instance, the pressure-rise curve downstream of a backward-facing step exhibits a self-similar trend as long as the boundary layer is thin (Adams and Johnston 1988). Furthermore, similarity or Reynolds independence of the velocity and Reynolds stress field was found before in the previous wake-flow studies (Merz et al. 1978; Nadge and Govardhan 2014).

The current results seem to be in line with these observations. The incoming boundary-layer thickness can be considered as thin ( $\delta_{99}/h < 0.4$ , Table 2), and thus, the inflow conditions comply with the restriction for similarity (Adams and Johnston 1988). The results, to be more specific the mean and turbulent flow quantities, indicate such self-similar characteristics with respect to the flow distribution as found in the literature. This seems to apply over the Reynolds and Mach number range under investigation. Thus, viscosity or compressibility effects might play a small role for the cases at hand.

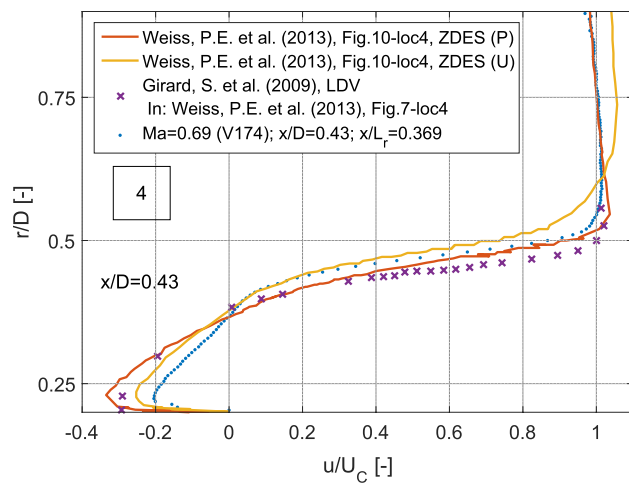


**Fig. 18** Streamwise mean-flow velocity profiles in the wake for Mach 0.7

### 3.2.4 Detailed comparisons with literature

Section 3.1 raised the question of what is the impact of the relatively high incoming turbulence level imposed by the ambient flow of VMK. To approach that question, comparisons to the literature are drawn. Weiss and Deck (2013) investigated a configuration very similar to the current one for an ambient flow at Mach 0.7. In principle, all aspects of the flow are similar except for the incoming turbulence. In this (mostly) numerical study, it is in the range of 0.5%, and thus, very small in comparison to the current experiment. Consequently, the effect on the turbulent quantities in the wake flow can be assessed. This is done by comparing radial slices of the mean and turbulent fluctuations for one exemplary axial position in the recirculation bubble ( $x/D = 0.43$ ,  $x/L_r = 0.369$ ).

As introduced, the experimental data are based on Laser Doppler Velocimetry (LDV) measurements by Girard et al. (2009). The corresponding numerical simulations by means of Zonal Detached Eddy Simulation (ZDES) consider two different conditions: a perturbed (*P*) and unperturbed (*U*) case. The perturbed case describes the situation as given in the wind-tunnel environment with a wind-tunnel nozzle and the unperturbed case reflects flight-like conditions. In other words, the impact of the test environment on the measurement results is assessed for an upstream supported wind-tunnel model in an open test section.

Figures 18, 19 and 20 depict the mean velocity, the turbulent intensity, and the Reynolds shear stress. Due to the spatial resolution of the thin shear layer (at  $r/D \sim 0.46$ ), the Reynolds shear stress at that axial location is certainly insufficiently resolved (remember that the comparison of the wake is the objective here; spatially higher resolved data were acquired by means of the FOV2). However, despite

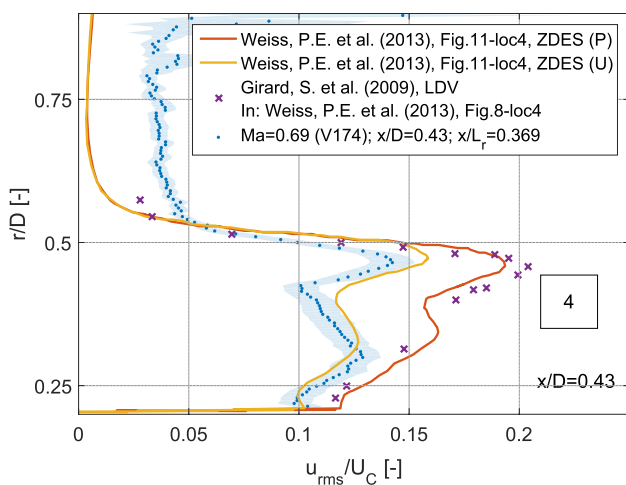


**Fig. 19** Axial turbulence intensity profiles in the wake for Mach 0.7

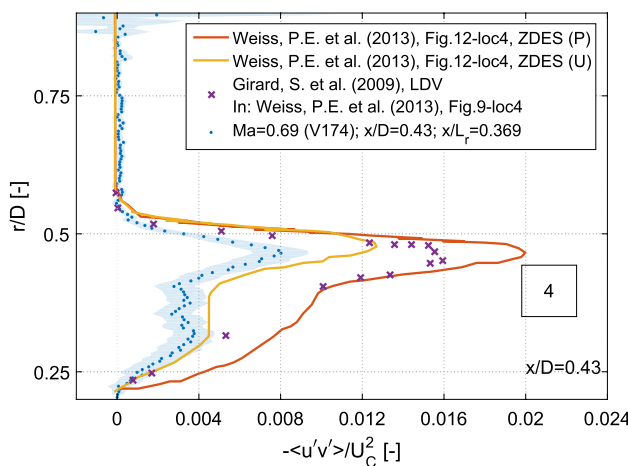


**Fig. 20** Streamwise Reynolds shear stress profiles in the wake for Mach 0.7

the differences between current experiment and reference simulation regarding the upstream turbulence, all the other quantities actually agree very well with the unperturbed case ( $U$ ) by Weiss and Deck (2013). In detail, the mean difference between the current results to the unperturbed results by Weiss and Deck (2013) amounts to  $|\Delta u/U_C| = 0.046$ ,  $|\Delta u_{\text{rms}}/U_C| = 0.011$ , and  $|\Delta \langle u'v' \rangle / U_C^2| = 0.002$  between  $0.2 < r/D < 0.5$ . The statement regarding the good agreement can be made for the exemplary slices at hand, but also for further slices, which have been used for the in-house validation of the current data set. Two conclusions might be drawn from that, which are presented in the following: the first regarding the influence of the incoming turbulence and the second regarding the perturbation introduced by the wind-tunnel facility.

VMK provides under the present conditions an inflow with a relatively high level of inflow turbulence between

3.5% and 2.4% for Mach 0.5 and 0.9 (Table 2), respectively. Nevertheless, the comparison shows a good agreement. It appears that the turbulent processes in the shear layer and wake might not be significantly influenced by the incoming turbulence level and/or indicates to have only a minor influence on the dynamics of the wake flow. A possible explanation might be that the time and length scales of the incoming turbulence and the wake-flow turbulence differ notably, and thus, could be independent from each other.

Weiss and Deck (2013) found crucial differences due to the influence of the test section ( $P$ ). The difference was attributed to the observation that a strong interaction between the inner and outer mixing layer takes place. The inner mixing layer here denotes the shear layer from the model, while the outer is given by the shear layer evolving from the trailing edge of the wind tunnel nozzle. The idea is that pressure waves emanate from the pairing process of the two shear layers, which cause a dampening of the spectral content. For the current study, nothing can be stated about the spectral content as the measurements have a low acquisition frequency. However, the footprint of the interacting shear layers has been noticed in the corresponding study (Weiss and Deck 2013) in the Reynolds stress results (Figs. 19, 20). The current results tend to be closer to the unperturbed case. This obviously does not exclude an influence of VMK, but its impact seems to be lesser. One reason might be that the diameter ratio between wind tunnel nozzle and model is 2.86 in Weiss and Deck (2013), while the current setup features a ratio of 5.1. In terms of the area ratio, it is 8.2 (Weiss and Deck 2013) vs. 26.0 (VMK config.).

Above, a good agreement (Figs. 18, 19, 20) was found with the unperturbed or free-flight results by Weiss and Deck (2013). An overview to results extracted from further readings are listed in Table 4. In general, all of those studies investigate an axisymmetric backward-facing step configuration of an Ariane 5-like geometry in the transonic flow regime without jet. Differences exist regarding the methodological approach, meaning CFD or experiment, geometrical variations, the model support method, etc. The conditions in Weiss and Deck (2013), however, resemble most closely the conditions at hand; most notably with respect to the base geometry and the upstream support.

Despite the similarities regarding the setup, the overview reveals a wide range of results regarding the maximum magnitude of turbulent quantities. The Reynolds shear stress for instance does not feature a significant difference to the unperturbed ( $U$ )/free-flight numerical results by Weiss and Deck (2013). However, a factor of about 1.5 can be found for the experimental and for the perturbed numerical results by the same study, which corresponds to the findings by Schrijer et al. (2014). A factor of 2 or larger is found in Scharnowski et al. (2015) for both CFD and experiments. The same proportions can be found for the turbulent intensity if

the power of the signal, meaning the squared magnitude, is considered.

Sub-grid filtering of small velocity quantities does not seem to responsible for the deviation. Scharnowski (2013) determines the Reynolds stresses by means of ensemble- and window-correlation-based evaluation schemes. The spatially higher resolved ensemble correlation features larger Reynolds stress level, but the deviation is of order of 5% maximally. Note that the spatial resolution of the current setup (*FOV1*) is slightly higher than the one used by Scharnowski (2013) for the window-correlation-based scheme.

Table 4 lists further potential influences for the deviation. Above, the impact of the inflow turbulence was hypothesized as negligible. That essentially leaves us with the conditions of the incoming boundary layer and the conditions imposed by the test environment. The incoming boundary layer mainly determines the evolution of the shear layer and its nature of impingement, meaning fluidic or on a solid wall. van Gent et al. (2017) investigated these differences by varying the nozzle length. In fact, it was found that a reattachment on a solid wall leads to a smaller level of turbulent quantities. In terms of the turbulent kinetic energy, the deviation can amount to a factor of about 1.3.

Regarding the test environment: as discussed above, Weiss and Deck (2013) investigated, by means of CFD, the influence of the 'open test section' wind tunnel for an upstream supported wind-tunnel model and compared the results to a free-stream configuration. It was shown that perturbations arise from interaction of the shear layer from the wind-tunnel nozzle and the wind tunnel model. Thus, the impact of the test conditions on the results was quantified and the sources for perturbations identified. The current results appear to be consistent with these observations. Furthermore, an influence is also expected from the other support systems. An overview to examples in the literature is given in Table 4. It is very unlikely that a strut in the vicinity of the base does not have an influence on the wake flow. Upstream traveling waves must also be induced for a sting–strut combination. Furthermore, a configuration featuring a sting is not equivalent to a configuration with a finite dummy nozzle. In summary, for both complementary 'support system' cases, the influence of the support system and test environment remains unclear/unspecified, meaning that the study by Weiss and Deck (2013) contributes substantially to the assessment of perturbations for the upstream supported case.

### 3.3 Shear-layer evolution

The incoming boundary layer experiences a flow separation at the shoulder of the base. This is the starting point for the development of the mixing layer with turbulent structures that grow in size and intensity in the streamwise direction.

Since the dynamics of the shear layer significantly influences the wake dynamics the evolution of which is often cited in the literature. For this reason and to support the reattachment scaling approach, the shear-layer evolution is shown next. Typically, the evolution is characterized by means of the vorticity thickness  $\delta_\omega$  as given in Eq. 5. Comparisons with the literature are drawn in Sect. 3.3.2.

#### 3.3.1 Vorticity thickness

The vorticity-thickness evolution for a shear layer with reattachment on a solid wall can usually be divided into three segments: the first segment is described by an initial exponential growth in the region where the shear layer develops up to about  $x/L_r \sim 0.3$  (Deck and Thorigny 2007; Simon et al. 2007). In succession, a second segment with linear spreading rate is to be expected that reaches a plateau (third segment) at about  $x/L_r \sim 0.6$ –0.7 if approaching obstructing elements such as a solid wall or a jet. In some studies, the initial exponential growth region is more pronounced (Deck and Thorigny 2007; Simon et al. 2007) than in others where they are barely notable (Statnikov 2016; Statnikov et al. 2016; Brown and Roshko 1974).

Figure 21 shows the vorticity-thickness evolution in the streamwise direction for the investigated Mach numbers and for both field of views. Note that the determination of the vorticity thickness is restricted to a range above the surface of the dummy nozzle ( $r/D \geq 0.2$ ). The results appear to support the reattachment length scaling concept, since the trends closely align for all Mach numbers. Close to the separation at about  $x/L_r \sim 0$ , the measurement results for *FOV2* are favored due to the higher spatial resolution. There, as in the previous citations (Statnikov 2016; Statnikov et al. 2016; Brown and Roshko 1974), the vorticity-thickness evolution

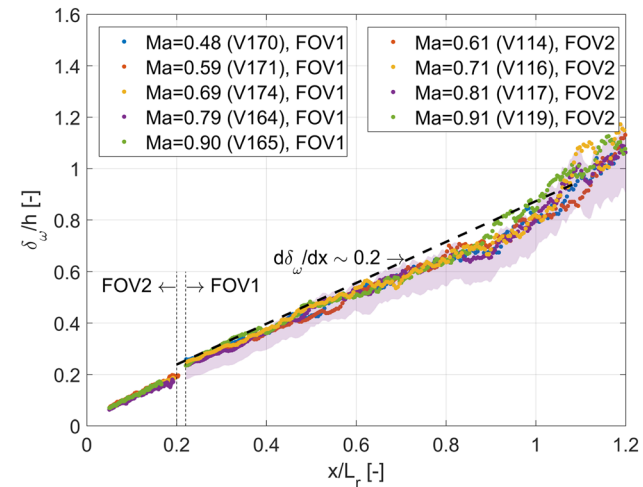


**Fig. 21** Streamwise vorticity thickness evolution for the investigated Mach numbers

does not show a notable exponential growth; it appears linear instead.

Keep in mind though that the shear layer closest to the base ( $x/L_r = 0.05$ ) is only resolved with five independent grid points (*FOV2*). Thus, due to the relatively strong velocity gradient changes over the shear layer, the determination of the maximum velocity gradient  $\partial u / \partial y$  as part of the equation for the vorticity thickness (Eq. 5) might suffer of subgrid filtering effects. This explains the offset of the vorticity thickness between *FOV2* and *FOV1*. At  $x/L_r = 0.2$ , *FOV2* resolves the shear layer with about 15 independent grid points, while only five independent grid points are available for *FOV1*. As a result, the velocity gradient is underestimated, and is, consequently, incorporated as part the error bar bounds for the Mach 0.8-case (V164) as background shading.

A linear trend is notable farther downstream (at  $x/L_r \geq 0.3$ ) where the spreading rate  $\delta_\omega/h$  is calculated to be in the range of 0.2, which is comparable with Schrijer et al. (2014) (see Sect. 3.3.2). A decrease of the vorticity-thickness growth appears to occur at  $x/L_r \geq 0.6$ , but the curve is far from developing a plateau. Instead, the current vorticity-thickness evolution features an amplified growth for  $x/L_r \geq 0.9$ . This might be associated with the finite length of the dummy nozzle: Downstream from the dummy nozzle end, the shear layer appears to have space to keep on growing in both directions, inwards and outwards.

### 3.3.2 Detailed comparisons with literature

The shear-layer evolution of the current results (Mach 0.7 and 0.8) is related in Fig. 22 to the findings in the literature (Statnikov 2016; Schrijer et al. 2014; Deck and Thorigny 2007). Close to the separation, the results show a good agreement with Deck and Thorigny (2007). A deviation can be noted in the area where the shear-layer growth is not influenced by the effects of the reattachment process. Deck and Thorigny (2007) report a growth rate of 0.38 for an axisymmetric configuration. Statnikov (2016) finds 0.27 for the axisymmetric backward-facing step configuration with sting. The spreading rate at hand is comparable to the results by Schrijer et al. (2014), which is the most similar configuration in terms of the base geometry: both feature a dummy nozzle. The overall vorticity-thickness evolution is also similar if the error bars are taken into account. Nevertheless, it is at a different level, which might be a result of different incoming boundary-layer thicknesses. Above, the absence of a plateau as shown in the numerical literature results was associated with the spatial limitation of the flow obstructing element. Note that Brown and Roshko (1974) revealed a spreading rate of 0.181 for generic splitter plate experiments with uniform density and zero velocity on the low speed side. In summary, a large range of spreading rates

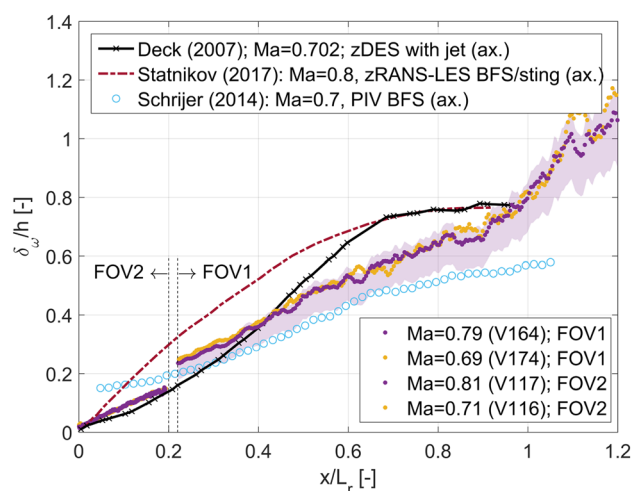


**Fig. 22** Streamwise vorticity-thickness evolution in comparison with results from the literature. Abbreviations/explanations: *zDES* zonal detached eddy simulation; *zRANS* zonal Reynolds Averaged Navier–Stokes simulation; *LES* large eddy simulation; *BFS* backward-facing step; *ax./planar* axisymmetric/planar configuration

are found in the literature. The difference might be explicable with the nature of reattachment: solid/obstructed by the jet, hybrid, or free. The spreading rate at hand resembles most closely the findings by Schrijer et al. (2014).

## 4 Conclusion and outlook

A generic space launcher was investigated experimentally in the vertical test section Cologne by means of PIV for subsonic Mach numbers ranging from about 0.5 to 0.9 for Reynolds numbers between  $0.8 \times 10^6$  and  $1.7 \times 10^6$ . The investigations focused on the question if a reattachment length-based scaling reveals the self-similar base-flow features. This was assessed by analyzing the mean and the turbulent flow fields. Furthermore, data to the incoming boundary layer and to evolving shear layer were provided. All data sets have been compared to the literature.

It was found that the results for the boundary layer, shear layer, and wake flow agree well with findings described in the literature (Klebanoff 1955; Schrijer et al. 2014; Weiss and Deck 2013). Deviations to the other sources (Schrijer et al. 2014; Scharnowski et al. 2015) regarding the turbulent velocity distribution might be explained by the nature of the shear-layer reattachment, meaning solid, hybrid, or fluidic (van Gent et al. 2017). Furthermore, upstream effects induced by pairing of shear layers or the interaction with the support system might contribute to the differences, but are speculative without further information. Again, focusing on the research question, evidences for the validity of such a reattachment length-based scaling seem to be present.

Overall, the mean-flow velocity distribution and the vorticity thickness appear comparable for all Mach numbers for this scaling approach and the same is indicated for the turbulent velocity quantities upstream from the reattachment location. In the vicinity of the dummy nozzle exit, differences are notable which might be explained by the abrupt geometry change. Finally, the results and the comparisons indicate that the influence of the incoming turbulence on the wake dynamics appears to be small. This observation is relevant for further base-flow interaction experiments in the vertical test section Cologne (VMK).

Next, the experiments with an overexpanded, cold supersonic exhaust jet will be analyzed. Complementary, the pressure signal of the current experiments will be evaluated with respect to its spectral content and the PIV data will be analyzed by means of proper orthogonal decomposition (POD).

**Acknowledgements** Financial support has been provided by the German Research Foundation (Deutsche Forschungsgemeinschaft DFG) in the framework of the Sonderforschungsbereich Transregio 40. Furthermore, thanks a lot to all colleagues and the staff for their support, especially to Dominik Neeb due to the good discussions in all matters.

**Open Access** This article is distributed under the terms of the Creative Commons Attribution 4.0 International License (<http://creativecommons.org/licenses/by/4.0/>), which permits unrestricted use, distribution, and reproduction in any medium, provided you give appropriate credit to the original author(s) and the source, provide a link to the Creative Commons license, and indicate if changes were made.

## References

- Adams EW, Johnston JP (1988) Effects of the separating shear layer on the reattachment flow structure; part 1: pressure and turbulence quantities. *Exp Fluids* 6(6):400–408
- Benedict L, Gould R (1996) Towards better uncertainty estimates for turbulence statistics. *Exp Fluids* 22(2):129–136
- Berg DE (1977) Surface roughness effects on the hypersonic turbulent boundary layer. Ph.D. thesis, California Institute of Technology
- Brown GL, Roshko A (1974) On density effects and large structure in turbulent mixing layers. *J Fluid Mech* 64(4):775–816
- Clauser FH (1956) The turbulent boundary layer. *Adv Appl Mech* 4:1–51
- David S, Radulovic S (2005) Prediction of buffet loads on the Ariane 5 afterbody. In: 6th Symposium on launcher technologies. Munich (8–11 November 2005)
- Deck S, Thorigny P (2007) Unsteadiness of an axisymmetric separating-reattaching flow: numerical investigation. *Phys Fluids* 19(6):065,103
- Deprés D, Reijasse P, Dussauge J (2004) Analysis of unsteadiness in afterbody transonic flows. *AIAA J* 42(12):2541–2550
- Girard S, Jordan P, Delville J, Fourment C, Royer A, Kerherv F, Braud P, Laurent P, Huet P (2009) Étude Expérimentale des Instabilités Aérodynamiques des Écoulements de Culot. Mesures Couplées Pression-Vitesse. Final LEA Report, Convention ONERA No F/11706/DA LROC
- Klebanoff P (1955) Characteristics of turbulence in boundary layer with zero pressure gradient. National Advisory Committee for Aeronautics, Report 1247, National Bureau of Standards
- Lazar E, DeBlauw B, Glumac N, Dutton C, Elliott G (2010) A practical approach to PIV uncertainty analysis. In: 27th AIAA aerodynamic measurement technology and ground testing conference, Chicago, Illinois
- Lê THH (2005) Étude expérimentale du Couplage entre l'Écoulement Transsonique d'Arrière-Corps et les Charges Latérales dans les Tuyères Propulsives. PhD thesis, Université de Poitiers, École Nationale Supérieure de Mécanique et d'Aérotechnique
- Mabey DG (1972) Analysis and correlation of data on pressure fluctuations in separated flow. *J Aircraft* 9(9):642–645
- Meliga P, Sipp D, Chomaz JM (2010) Effect of compressibility on the global stability of axisymmetric wake flows. *J Fluid Mech* 660:499–526
- Merz R, Page R, CEG P (1978) Subsonic axisymmetric near-wake studies. *AIAA J* 16(7):656–662
- Murthy S, Osborn J (1976) Base flow phenomena with and without injection—experimental results, theories, and bibliography. *Aerodynamics of base combustion(A 76-37230 18-02)* New York, American Institute of Aeronautics and Astronautics, Inc pp 7–210
- Nadge PM, Govardhan R (2014) High Reynolds Number flow over a backward-facing step: structure of the mean separation bubble. *Exp Fluids* 55(1):1657
- Raffel M, Willert CE, Wereley S, Kompenhans J (2013) Particle image velocimetry: a practical guide. Springer, New York
- Roshko A, Lau JC (1965) Some observations on transition and reattachment of a free shear layer in incompressible flow. In: Charwat AF (ed) Proc 1965 Heat Transfer and Fluid Mechanics Institute. Stanford University Press, Stanford, pp 157–167
- Saile D, Kirchheck D, Gültan A, Banuti D (2015) Design of a hot plume interaction facility at DLR cologne. In: Proceedings of the 8th European symposium on aerothermodynamics for space vehicles, Lissabon, Portugal
- Scharnowski S (2013) Investigation of turbulent shear flows with high resolution PIV methods. Ph.D. thesis, Universität der Bundeswehr München, Fakultät für Luft- und Raumfahrttechnik
- Scharnowski S, Statnikov V, Meinke M, Schröder W, Kähler CJ (2015) Combined experimental and numerical investigation of a transonic space launcher wake. *EDP Sci* 7:311–328. <https://doi.org/10.1051/eucass/201507311>
- Scharnowski S, Bolgar I, Kähler C (2016) Interaction of a generic space launcher wake with a jet plume in sub-, trans- and supersonic conditions. In: International workshop on non-intrusive optical flow diagnostics
- Schetz J, Bowersox R (2011) Boundary layer analysis. In: AIAA education series. American Institute of Aeronautics and Astronautics. <https://books.google.de/books?id=GhkqYAAACAAJ>
- Schröder F, Sciacchitano A, Scarano F (2014) Spatio-temporal and modal analysis of unsteady fluctuations in a high-subsonic base flow. *Phys Fluids* 26(8):086,101
- Schwane R (2015) Numerical prediction and experimental validation of unsteady loads on ARIANE 5 and VEGA. *J Spacecr Rockets* 52:54–62
- Simon F, Deck S, Guillen P, Sagaut P, Merlen A (2007) Numerical simulation of the compressible mixing layer past an axisymmetric trailing edge. *J Fluid Mech* 591:215–253
- Statnikov V, Bolgar I, Scharnowski S, Meinke M, Kähler C, Schröder W (2016) Analysis of characteristic wake flow modes on a generic transonic backward-facing step configuration. *Eur J Mech B/Fluids* 59:124–134
- Statnikov V, Meinke M, Schröder W (2017) Reduced-order analysis of buffet flow of space launchers. *J Fluid Mech* 815:1–25. <https://doi.org/10.1017/jfm.2017.46>
- Statnikov V (2016) Numerical analysis of space launcher wake flows. Ph.D. thesis, Rheinisch-Westfälische Technische Hochschule Aachen, Fakultät für Maschinenwesen

- Uberoi MS, Freymuth P (1970) Turbulent energy balance and spectra of the axisymmetric wake. *Phys Fluids* 13(9):2205–2210
- van Gent P, Payanda Q, Brust S, van Oudheusden B, Schrijer F (2017) Experimental study of the effects of exhaust plume and nozzle length on transonic and supersonic axisymmetric base flows. In: 7th European conference for aeronautics and space sciences, Milan, Italy
- Weiss P, Deck S (2013) Numerical investigation of the robustness of an axisymmetric separating/reattaching flow to an external perturbation using ZDES. *Flow Turbul Combust* 91(3):697–715
- Weiss PE, Deck S, Robinet JC, Sagaut P (2009) On the dynamics of axisymmetric turbulent separating/reattaching flows. *Phys Fluids* 21(7):075,103
- Westphal RV, Johnston J, Eaton J (1984) Experimental study of flow reattachment in a single-sided sudden expansion. NASA Contractor Report 3765
- White F (1991) Viscous fluid flow. McGraw-Hill Series in Mechanical Engineering, McGraw-Hill. <https://books.google.de/books?id=G6IeAQAAIAAJ>
- Wolf CC (2013) The subsonic near-wake of bluff bodies. Ph.D. thesis, Rheinisch-Westfälische Technische Hochschule Aachen, Fakultät für Maschinenwesen

**Publisher's Note** Springer Nature remains neutral with regard to jurisdictional claims in published maps and institutional affiliations.

## Affiliations

Dominik Saile<sup>1</sup>  · Viktor Kühl<sup>1</sup> · Ali Gülnan<sup>1</sup>

 Dominik Saile  
dominik.saile@dlr.de

<sup>1</sup> Institute of Aerodynamics and Flow Technology, Supersonic and Hypersonic Technologies Department, DLR German Aerospace Center, Linder Höhe, 51147 Cologne, Germany